THUNDER HORSE INJECTION PUMP

by

Paul Meuter

Global Product Development Manager Oil & Gas

Wolfram Lienau

Manager Analysis and Mechanics

Thomas Felix

Analyst Engineer

Andreas Schachenmann

Vice President Product Development

Sulzer Pumps Ltd.

Winterthur, Switzerland

Brian Germaine

Deputy Engineering Director

Sulzer Pumps (UK) Ltd.

Leeds, United Kingdom

and

Charles L. McDonald

Senior Rotating Equipment Engineer

BP Amoco Corporation

Houston, Texas

Paul Meuter is Head of the Design and Product Development Group of Sulzer Pumps Ltd., in Winterthur, Switzerland, and is also responsible for product development of the Oil & Gas segment. In 1980, he joined Sulzer Pumps as a Design Engineer for pumps in the power industry. After stays at Sulzer Pumps in Leeds, United Kingdom, and in Portland, Oregon, where he had various positions in the engineering departments, Mr. Meuter rejoined Sulzer Pumps in Winterthur at his current position. His group's activity is in the field of design and development of special injection, multiphase, pipeline, and boiler feed pumps.

Mr. Meuter graduated with a degree (Mechanical Engineering, 1979) from Zurich Technical College.

Wolfram Lienau is Head of the Analysis and Mechanics Group of Sulzer Pumps Ltd., in Winterthur, Switzerland. After working three years as a teaching assistant at the Technical University Darmstadt, he joined the R&D division of Eastman Christensen, a drilling tool manufacturer, located in Celle, Germany. Mr. Lienau's activities included the strength calculation of drilling tools and the mechanical behavior of drill pipes, mainly by means of finite element analyses. In 1990, he moved to Sulzer Innotec as the Head of the Structural Mechanics group. Sulzer Innotec supported the product divisions of the Sulzer technology corporation with engineering services and R&D projects. Mr. Lienau joined Sulzer Pumps in 2000. The Analysis and Mechanics Group provides Sulzer Pumps' groups worldwide with engineering services as well as with R&D activities.

Mr. Lienau received his master diploma (Mechanical Engineering) from the Technical University in Braunschweig.

Thomas Felix is Analyst Engineer in the Analysis and Mechanics Group of Sulzer Pumps Ltd., in Winterthur, Switzerland. He joined Sulzer Pumps in 1995. After having worked for four years in the Engineering Department of Sulzer Pumps, in São Paulo, Brazil, he rejoined the Mechanics Group in Winterthur. His group's activity is in the fields of rotordynamics, stress calculations, and finite element analyses.

Mr. Felix graduated with a degree (Mechanical Engineering, 1994) from Magdeburg Technical University.

ABSTRACT

For the "Thunder Horse" oil field, injection pressures above 550 bar (8000 psi) are required. The highest injection pressures realized up to now with centrifugal pumps were around 350 bar (5100 psi).

To minimize the considerable risk of using unproven new technology, the oil companies involved decided to fund an initial feasibility study with several pump manufacturers to determine the best possible solution with the least technical risk. After a thorough evaluation of the various designs, a first full scale prototype pump was ordered, built, and tested.

All designs were verified by extensive testing of the first executed pump. The tests confirmed the suitability of the design, rotordynamic integrity, and the accuracy of the hydraulic performance.

INTRODUCTION

In recent years in the Gulf of Mexico oil exploration has been moving farther offshore into deeper water. Understanding the challenges that these new prospects will pose to production facilities and being able to address these challenges will determine the level of success of the oil production facility. One such example of these challenges is the use of water injection for primary recovery to support reservoir pressure maintenance.

The Thunder Horse Oil Field (Figure 1), 125 miles off the coast of New Orleans, is the largest oil field ever found in the United States' Gulf of Mexico. Experts now estimate that there are upward of three billion barrels of oil waiting to be claimed. Two oil companies, BP and ExxonMobil, have formed a partnership to develop this huge deposit. Situated at a water depth of more than 2000 m (6000 ft), the site requires injection pressures for recovery higher than ever done before.

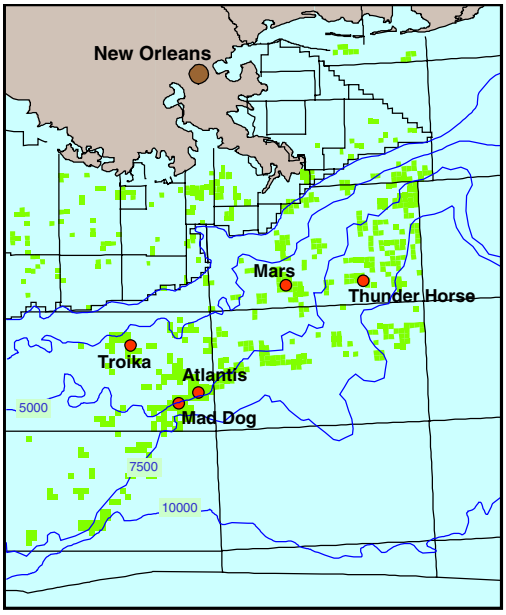

Figure 1. Leading Deep Water Lease Position.

Water injection is a crucial component to oil production offshore. By supporting the volume replacement from producing oil with water, the reservoir pressures can be maintained, thus improving the oil recovery from the reservoir. By producing oil from deeper water, the reservoir pressure is at higher levels than experienced in the past. This translates to water injection pumps that are required to deliver quantities of water at higher pressure than have been accommodated in the past and hence, dictating centrifugal pump technology being advanced past existing technology and experience. BP Thunder Horse Project currently has an application for water injection at 586 bar (8500 psi). With this application outside the limits of existing technology, the approach to addressing this challenge needs to be well thought out and executed such that impact on production efficiency is minimized. Robust design, reliability, and qualification testing are areas that need to be addressed in detail to understand the implications to the design and the production facility.

Because seawater injection is vital to the project's success, the oil companies took the unprecedented step of funding several pump companies to develop designs to meet the special needs of this field. The oil companies then evaluated the designs submitted and chose one design to be developed further. After thorough design reviews, a contract to manufacture and test one prototype pump was then given to the selected pump manufacturer. In the following chapters the steps from design to execution and test are detailed.

CUSTOMER'S REQUIREMENT

Safety and Reliability

The oil companies recognized very early in the project that the injection pressure requirements were far beyond those previously experienced within the industry. In order to limit the risk, the oil companies established the following criteria:

- The water injection pumps are critical to the timing of the project and the platform's overall uptime.
- It is a requirement that the water injection pumps be highly reliable and safe.
- Efficiency is important due to the large horsepower required, however, a small sacrifice in efficiency would be preferred over *any* sacrifice in reliability.
- Therefore the pump design must consider reliability and the ability to operate the pumps safely as the two highest priorities.

Operating Points

The customer specified head and flow only. Although gas turbine and variable frequency motor drives with and without gearboxes were evaluated as driving systems, no decision was taken at that time, meaning that the speed was not fixed (Table 1).

Table 1. Specified Head and Flow.

	rated (1)	rated (2)
Flow (m^3/h), (GPM)	497.4 (2190)	331.14 (1458)
Head (m), (ft)	4158 (13,640)	5633 (18,480)

PUMP SELECTION

The head was far higher than any head achieved in modern seawater injection pumps before and demonstrated the biggest challenge. The dictating parameters for generating high heads are speed and number of stages. It was obvious that existing parameters had to be exceeded but without compromising safety and reliability. Two speeds were chosen for a parameter study. 8500 rpm was the speed for the direct gas turbine drive and 6000 rpm for gas turbine/gearbox or a motor/gearbox drive. Two operating points had to be met. Therefore, the best efficiency point was selected between the two operating points. The variable speed drive allowed operating the pump at reduced speed to meet the second operating point. A series of existing hydraulics proven for high head applications were available from which we had to choose. They ranged from nq 22 (ns 1137) to nq 33 (ns 1705). Lower specific speed hydraulics would reduce the efficiency considerably. With all the above in mind, three different options out of six have been selected for further investigations. The three options are shown in Table 2.

Table 2. Investigated Design Options.

	Option		
	1	2	3
Speed (RPM)	8500	6000	8500
Specific speed nq (ns)	27 (1395)	22 (1137)	22 (1137)
Number of stages	10	12	8
Head per stage (m), (ft)	563 (1847)	470 (1542)	704 (2310)
Impeller diameter (mm), (in)	220 (8.7)	285 (11.2)	250 (9.8)
Impeller arrangement	Back-to-back	Back-to-back	inline
Design concept	(B)	(B)	(A)

Design Concept (A)

The design with all impellers arranged inline (Figure 2) is the classical design concept used on most of the high power multistage pumps either for injection or boiler feed service. A balance drum installed after the last stage reduces the axial hydraulic thrust to the capacity of the double acting thrust bearing. Normally, mechanical

seals on the drive-end (DE) and nondrive-end (NDE) sides seal the suction pressure to atmosphere. Pressure oil feed journal and thrust bearings align the rotor to the stationary casing. The pump is designed with a full pullout cartridge allowing a quick exchange of the cartridge. The mechanical seal can be changed without removing the cartridge since a spacer type coupling is utilized.

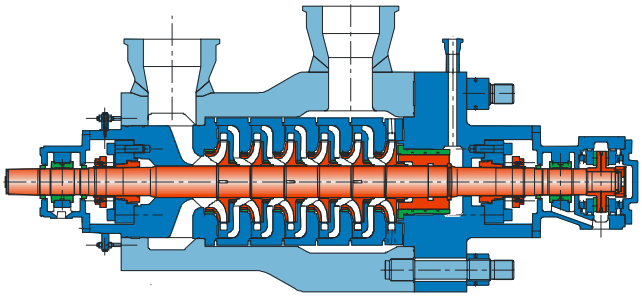

Figure 2. Design Concept (A), Inline Design.

Design Concept (B)

Opposed impeller designs (also called back-to-back designs) have been known for a very long time (Figure 3). Two groups of impellers are arranged opposite to each other, balancing the axial hydraulic thrust and requiring a much smaller thrust bearing as design (A). The center bushing and the throttle bushing are only subjected to half the total pump pressure and act as Lomakin type bearings. This design is especially suited for pumps with a high number of stages. This design is used mainly in volute style pumps with an axially split inner case. For very high pressure a diffuser style pump is preferred since the radially split inner case is easier to seal, the barrel casing is smaller in diameter, and thus also easier to seal and manufacture. During operation, the pressure to be sealed to the atmosphere is the pressure generated from the first set of impellers, which is about half the discharge pressure. All other design features are the same as for design (A).

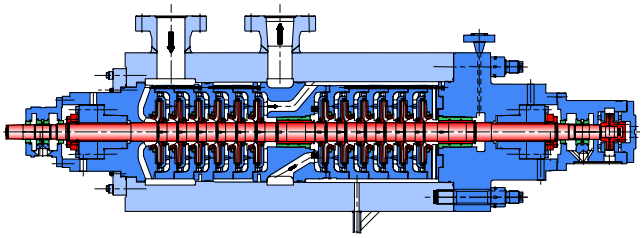

Figure 3. Design Concept (B), Back-to-Back Design.

Designer's Experience

All three options had been evaluated in view of the designers experience and the imposed standards such as API 610, Eighth Edition (1995). For this purpose, rough design layouts had been developed.

Speed

There are boiler feed pumps operating successfully at a speed of 8500 rpm but with a maximum of four stages. The rotordynamic analysis would show if an eight-stage pump could be built to the design concept (A). There are many eight-stage pumps in operation but with speeds lower or equal to 6000 rpm. There are pumps in operation built to the design concept (B) at speeds of 6000 rpm with up to 16 stages.

Head per Stage

The head per stage for seawater injection pumps has been limited for reasons of erosion/corrosion in the impellers and diffusers. Material tests for different water compositions and various flow velocities have been conducted by Weber (1987). The test results (Figure 4) show that for an austenitc-ferritic steel the allowable flow velocity is 55m/s (180 ft/s) if the material loss is kept below 2.1 g/m2*d = 0.1 mm/year (0.004 in/year). Materials are considered to be erosion/corrosion resistant below this value. The generated head per stage is about 600 m (1968 ft) for the flow velocity in the impeller side room of 55 m/s (180 ft/s). The eight-stage pump would be less favored in view of the erosion/corrosion resistance.

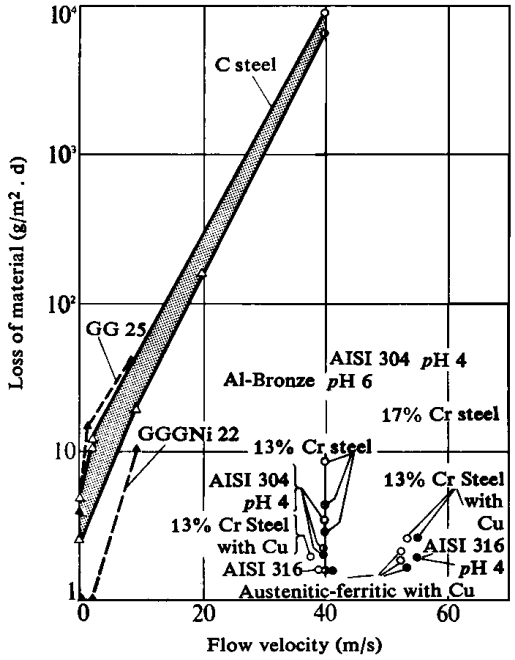

Figure 4. Erosion/Corrosion Test.

Hydraulics

The hydraulics are characterized by the specific speed. Hydraulics with the same specific speed can be enlarged or reduced following the affinity laws. Existing hydraulics were selected for the three options but, because of the high head, a thicker shaft was required to transmit the power. The increase in shaft diameter is a relatively small alteration and would affect only the net positive suction head (NPSH) and the efficiency slightly, but not the shape of the head-flow curve. All three options would be based on known hydraulics.

Shaft Stress

First, the torsional stress in the shaft end was checked. We found that the shaft stresses were too high with the standard hydraulics. This required increasing the shaft thickness. The designer's shaft calculation program was integrated with the lateral rotordynamic program using the same model and loading. The two most critical shaft sections have been checked for five different criteria. The goal was that the calculated stresses do not exceed the stresses of existing pumps in operation. This was achieved with all three options.

Design Pressure

Centrifugal injection pumps with such a high head had never been manufactured before. The designer had previously manufactured large barrel pumps with a hydrostatic test pressure of 720 bar (10440 psi) from which knowledge could be drawn. The main concern was the sealing of the barrel casing to the atmosphere and the manufacture of the barrel casing. The barrel casing had been calculated following the rules of ASME, Section VIII, Division 1,

as required by API 610 (1995). It was obvious that the smaller the impeller diameter, the smaller the barrel wall thickness and the bolting were. None of the options had wall thickness that could not be manufactured. Different sealing systems had been evaluated, and it became obvious that further development work was necessary for the selected sealing option.

Rotordynamics

All three options had been analyzed and compared following the criteria of API 610, Eighth Edition (1995). The analysis methods and the program are described in detail in the "DESIGN OF THE PROTOTYPE PUMP" section below. The damping diagram (Figure 5) showed satisfactory damping for all three options, but for worn clearances the modal damping of the pumps running at 8500 rpm dropped into the unacceptable region even with swirl brakes. The pump operating at 6000 rpm had high damping with and without swirl brakes. For the option (4) the frequency ratio was higher mostly because of the lower speed and the fact that the throttle and the center bushing gave enough support, not allowing the eigenfrequency to drop too much, although the rotor was longer and more slender.

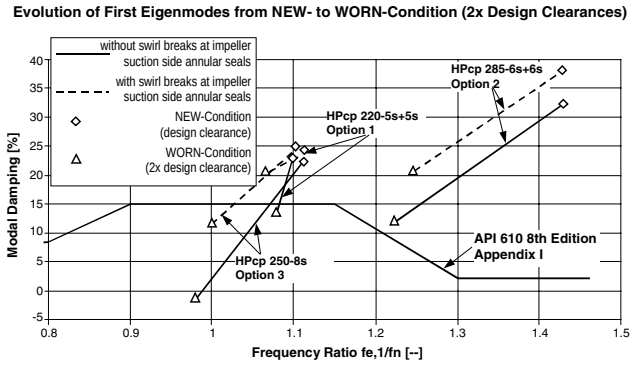

Figure 5. Damping Diagram for Options 1 to 3.

Mechanical Seals

Based on previous experience with produced water where calcium carbonate and sand caused problems, double mechanical seals for all three pump options had been planned for. At that stage only the p*v-value (Table 3) had been compared with pumps in operation. The suction pressure during normal operation was not high with 32 bar max (465 psi). The drive-end and the nondrive-end seals had the same pressure to seal for both design concepts (A) and (B). The p*v-values were within a reasonable range for all three options.

*Table 3. P*V-Value for Mechanical Seal.*

	Option		
	1	2	3
Speed (RPM)	8500	6000	8500
Sliding speed (m/s), (ft/s)	58 (190)	44 (144)	58 (190)
Sealing pressure (bar), (PSI)	32 (465)	32 (465)	32 (465)
p*v–value (bar m/s), (PSI ft/s)	1856 (88,350)	1408 (66,960)	1856 (88,350)

Axial Thrust and Bearing Size

Pumps having impellers arranged inline (design concept (A)) use a straight balance drum as an axial thrust-balancing device. Balance disks are not preferred because the axial sealing gap is much smaller than the radial gap of the balance drum, hence it is more sensitive to abrasive service. The balance drum is sized such that the double acting thrust bearing is loaded toward the outboard side while the clearances are in new condition. With increasing clearances due to erosion/abrasion, the inboard thrust bearing becomes loaded. This thrust change is high because the thrust generated in the impellers and the thrust balanced in the balance drum act differently with increasing wear, and, therefore, a large thrust bearing size is required with the design concept (A).

Pumps with opposed impeller arrangement have a much smaller thrust change since the opposed impellers balance the thrust themselves also with increasing wear in the clearances.

Sand Handling

Injection pumps must be capable of handling sand, especially if produced water is pumped. Most wear is expected in the close running clearances where the flow velocity is high. Hardly any information on the sand was available. For reasons of comparison the wear prediction model as described below and by Meuter, et al. (2000), was used. This assumed that the grain size of the sand was smaller than the radial clearance so no three-body abrasion would occur. All parameters had been left constant; only the flow velocity was varied. The material loss increases with the power of 3.4 of the velocity. This shows that it was important to keep the head per stage and thus the flow velocity as small as possible.

$$\delta = p^{*}\left(1+10\sin^{2}\varepsilon\right)^{*} c_{sq,eq}{}^{*} w^{3.4}{}^{*} G_{SF}{}^{*} F_{Mat} \qquad (1)$$

where:

δ	[mm/h]	=	Material loss rate
p	[-]	=	Constant
ε	[°]	=	Impact angle (parallel flow $\varepsilon = 0$)
$c_{sq,eq}$	[kg/m^3]	=	Equivalent quartz concentration
G_{SF}	[-]	=	Grain size factor
w	[m/s]	=	Relative flow velocity of fluid
F_{Mat}	[-]	=	Material factor

The flow velocities in the close running clearances of the impeller eye rings and balance drum, respectively center and throttle bushing, had been tabulated. The relative material loss had been calculated with the ratio of flow velocity to the power of 3.4 using the lowest flow velocity as reference. The results (Figure 6) showed clearly that the lowest wear could be expected with option 2.

			Option		
			1 5s+5s	2 6s+6s	3 8s
Diameter at center bush, resp. balance drum	Db	mm inch	125 4.92	143 5.63	150 5.9
Flow velocity through center bush, resp. balance drum	vb	m/s ft/s	82.4 270	79.3 260	108 354
Relative material loss in center bush, resp. balance drum	mlb	-	**1.14**	**1**	**2.85**
Diameter at impeller eye wear surface	Dil	mm inch	145 5.71	165 6.49	145 5.71
Flow velocity at impeller eye wear surface	vil	m/s ft/s	60.9 200	53.3 175	65.9 216
Relative material loss on impeller eye wear surface	mli	-	**1.57**	**1**	**2.06**

Figure 6. Sand Handling Capability.

Efficiency

Although efficiency was not considered to be a key factor to the project, it had been evaluated, too. The option with the highest specific speed hydraulic had the highest efficiency.

Weight and Size

Weight is always important on platform installations. Here only the pump weight had been compared although the driver system had a much higher impact.

Summary of Pump Selection

All above aspects had been compared and summarized in Figure 7. Four pluses were the highest rating. Rotordynamics were not

acceptable for option 3, and therefore this option had to be disregarded. The designer proposed option 2 because the speed, rotordynamic behavior, and the sand handling capability met the customer's requirements best in view of reliability. It was identified that during the design of the prototype pump, attention had to be paid to the tightness of the delivery cover/barrel casing joint, the tightness of the suction casing/barrel casing joint, and to the rotordynamics. Furthermore, the wear parts had to be protected from abrasives adequately to meet a reasonable life expectancy.

		Option		
		1 5s+5s	2 6s+6s	3 8s
Injection Pump Experience	Head per stage	+++	++++	+
	Existing hydraulics	++++	++++	++++
	Shaft stress	++++	++++	++++
	Speed	++	++++	++
	Design pressure	++	++	++
Rotor dynamics		++	++++	----
Mechanical seal		+	+++	+
Axial thrust bearing size		++++	++++	++
Capability of sand handling		+++	++++	+
Efficiency		++++	+++	+
Weight and size (pump only)		++	+	++++

Figure 7. Summary Pump Selection.

DESIGN OF THE PROTOTYPE PUMP

After the selection of option 2, the prototype pump was designed. Only the most relevant features are described here.

Establishing the Design Pressure

There is no standardized way in the industry of how design pressure is established. Finally we agreed on the method described below.

- Shut-off head = 6200 m (20,341 ft)
- Maximum density = 1050 kg/m^3 (SG = 1.05)
- Maximum suction pressure = 32 bar (465 psi)
- Five percent required head increase as per API 610, Eighth Edition (1995), paragraph 2.1.4, and + 5 percent test tolerance were considered.
- Calculated design pressure = (6200 * 9.81 * 1050 * 1.05 * 1.05 * 10^{-5}) + 32 = 736 bar (10,676 psi)

The suction as well as the discharge side including the intermediate pressure chamber had to be designed for the full 736 bar (10,676 psi).

Hydrostatic Test Pressure

API 610, Eighth Edition (1995), calls for a hydrostatic test pressure of 1.5 times design pressure. ASME, Section VIII, Division 1, UG-99, 1999, Addenda July 1, allows a hydrostatic test pressure of 1.3 times design pressure. Because of the very high design pressure, we agreed to follow the rules of ASME.

- Hydrostatic test pressure = 1.3 * 736 bar = 957 bar (13,881 psi).

PUMP DESIGN

Concept

The pump was designed according to the design concept (B) described earlier in the PUMP SELECTION section. Refer to Figure 8 for the design of the prototype pump. Components and features critical to reliability and safety had been identified during the design process for detailed investigations.

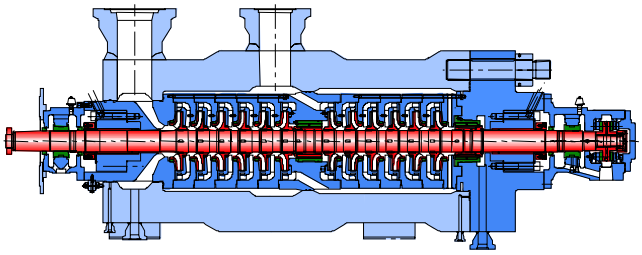

Figure 8. Prototype Pump Design.

Pressure Retaining Parts

The pressure retaining parts had been analyzed following the rules of ASME, Section VIII, Division 1, for the design pressure of 736 bar (10,676 psi). This analysis demonstrated that all primary stresses were within the limits, but did not provide distortions, peak stresses in notches, nor the contact force between the barrel casing and the delivery cover, vital to the tightness of the joint. Therefore, a finite element analysis of the subject components was required.

Static Seals

Critical to safety are all static seals sealing to atmosphere. An elastomeric O-ring seal, arranged between the delivery cover face and the barrel cover face, was installed. Face O-ring seals without backup rings are capable of sealing such high pressures if the joint has metal-to-metal contact at any operating condition, thus not providing an extrusion gap for the O-ring. To prove this, a finite element calculation was performed as described below.

The seal sealing the suction casing and the barrel casing to atmosphere had to be arranged radially for design reasons (refer to Figure 30). This seal was considered to be the most difficult seal, and no experience in the pump industry was at hand. The designer investigated several options from different seal manufacturers. The selected sealing system (Figure 9) was a proven seal combining a tough, resilient, T-shaped ring with pressure actuated antiextrusion rings for use with pressure ratings up to 3000 bar (43,500 psi) used in the aeronautic industry. This design prevents the elastomeric-sealing element from wedging into the diametrical clearances under pressure. The resilient T-shaped elastomeric sealing element deforms its flange instantaneously under pressure, lifting the antiextrusion ring on the low pressure side of the assembly to contact the bore, closing the extrusion gap before any extrusion of the sealing element can occur. The extrusion gap for hydrostatic test, design, and operating conditions resulted from the finite element calculations. Prior to manufacturing the prototype pump, a small test rig consisting of two rings with two seals was built and successfully tested at a hydrostatic test pressure of 957 bar (13,881 psi), simulating the same extrusion gap as in the prototype pump. This gave confidence that the seal system was working as intended.

Figure 9. Static Seal System for Suction Casing.

As an additional safety precaution, a "telltale" leakage detection had been included on the suction and delivery side to warn against any leakage across the inner O-ring seals.

Nozzle Connections

Standard ASME B16.5 type flanges were not acceptable because their pressure rating was too low even for the highest-class rating. The designer had used proven clamp type nozzle connectors before (Figure 10), which are available on the market for such high pressures. One end of the nozzle was integrated into the fabricated barrel casing. The metal-to-metal seal ring was designed as a pressure-energized bore seal concept and can be reused after disassembly.

Figure 10. Clamp Nozzle Connector for Suction and Discharge Nozzles.

Mechanical Seals

As mentioned before, double mechanical seals (Figure 11) had been selected with an externally circulating barrier fluid system. The question was if the mechanical seal had to withstand the full static discharge pressure. One of the pumps could be pressurized to this pressure when the check valve leaked and the suction valve was closed while the pump was on standby. Because of that situation, a double tandem seal arrangement had been selected. The seal faces of the inboard seal were subjected to external pressure and, hence, to compressive stresses if the described reverse pressure situation occurred. Where, on a conventional double mechanical seal in back-to-back arrangement, the seal faces would be in tension and therefore could not be pressurized as high.

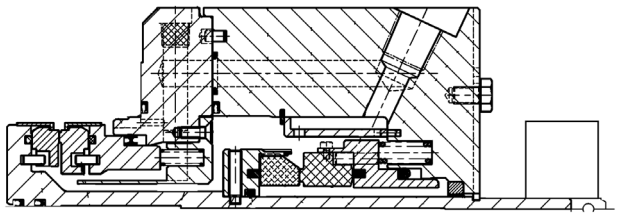

Figure 11. Mechanical Seal in Tandem Arrangement.

Axial Thrust and Thrust Bearing

The axial thrust had been analyzed using a computer code developed inhouse. The code is based on the theory and corrected for the hydraulic's specific flow regime and geometrical influences. These corrections had been derived from thrust measurements of actual pumps. The result is presented in Figure 12. With new condition clearances, the thrust was acting toward the pressure side (outboard). As the clearances wear, the thrust moved toward the suction side (inboard). On top of the calculated residual thrust, a safety margin and the small thrust of the flexible coupling were added to both sides. It was demonstrated that the residual thrusts were at any operating condition below the rated thrust bearing capacity. The impeller wear rings wear evenly throughout the pump, thus compensating the change in axial hydraulic thrust to a high degree. This is the advantage of the opposed impeller over the inline pump where the wear of the impeller wear rings and the balance drum is not self-compensating, and thus requires a much larger thrust bearing. A double acting self-equalizing tilting pad thrust bearing was used to absorb the residual thrust as specified by API 610 (1995). The pressure is fed directly into the pads and therefore generates less loss.

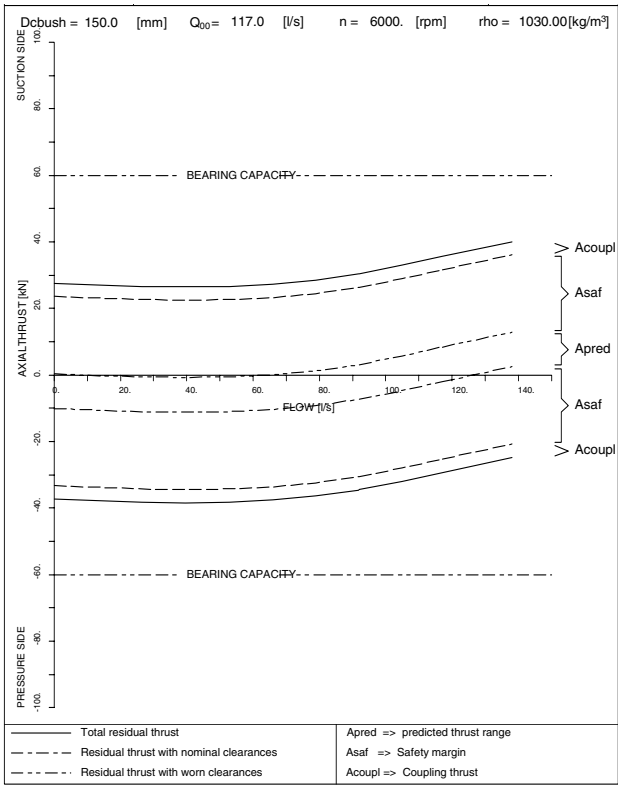

Figure 12. Residual Hydraulic Axial Thrust.

Sand Handling

The customer asked what the allowable sand concentration was and what wear part materials had to be used to achieve a satisfactory lifetime. To answer this question, the wear prediction model had been used. It was assumed that two years' mean time between overhauls was acceptable. After two years, the wear parts would be worn, meaning that the clearances would be twice new condition. It was assumed that most of the sand was quartz and that the particulates were smaller than the radial clearance. Good successes with WC Co Cr high velocity oxy fuel (HVOF) coatings in the impeller wear parts and solid tungsten carbide in the balance drum had been experienced (refer to Figure 2). The formula was solved for the sand concentration. The allowable sand concentration was tabulated in Table 4. Based on this estimation, it was decided to coat the integrated impeller wear surfaces and the stationary wear rings with the WC Co Cr HVOF coating and to install solid tungsten carbide sleeves and bushings in the center and throttle bushings. Special care had to be paid to the design of the center and throttle sleeves because the solid tungsten carbide does not have the same coefficient of thermal expansion as the shaft material, and because the material is brittle and therefore tensile stresses should be kept very low. On high head pumps, integrated wear surfaces are preferred over separate impeller wear rings because high axial hydraulic forces and rubs during operation, loosening the ring due to the generated heat, make it difficult to secure separate impeller wear rings safely.

Table 4. Estimated Allowable Sand Concentration.

Location	Stationary and rotating wear part material	Estimated allowable sand concentration (g/m^3)
Impeller eye ring	WC Co Cr HVOF coating	5.1
Center bushing, throttle bush	Welded overlay WC Ni-CrCo	0.81
	Solid tungsten carbide	10.5

Material of Construction

The material selection was based on the specified seawater and produced water compositions and on the designer's operation and manufacturing experience. Corrosion resistance and high strength were of importance. The forged super duplex stainless steel ASTM A182 Gr 53 was selected for all pressure retaining parts including barrel casing and delivery cover. The major concern was to keep the wall thickness of the barrel casing within known limits in order to ensure the mechanical properties and the corrosion resistance. For all internal cast parts, such as impeller diffusers and suction casing, the cast version of the super duplex stainless steel ASTM A 890 Gr 5A was selected.

Hydraulics

An nq 22 (ns 1137) hydraulic used in many pumps before was selected. The shaft for this standard hydraulic was too small to transmit the power. The shaft diameter had to be increased involving small changes at the impeller eye. Because of the importance of this pump, a four-stage model pump was built and tested confirming the pump performance prior to manufacturing of the prototype pump.

General Arrangement

The pump set is mounted on a baseplate, which is supported on three points on the platform deck (Figure 13). The overall width of the skid is 3.6 m (11.81 ft) and the overall length is 11.2 m (36.7 ft). The lube oil system is placed at the back of the pump with its major equipment placed on the sides to allow the extraction of the pump cartridge. The separate mechanical seal support API Plan 53 system is installed on the side of the pump supporting the DE and NDE seals. A 10 MW four-pole variable frequency motor drives the pump through a speed increasing gear.

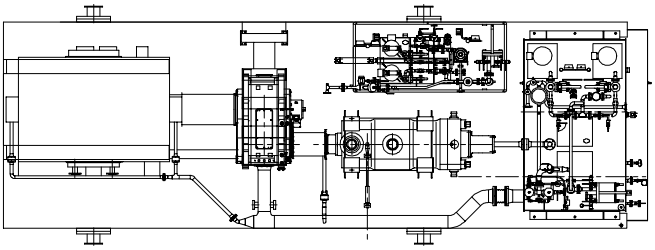

Figure 13. General Arrangement, with Motor, Gear, Pump, Lube Oil, and Mechanical Seal Support Systems.

FINITE ELEMENT ANALYSES

General

Finite element analyses were performed for design assistance. These analyses include the following parts and assemblies of the pump. The different objectives were:

- Rotordynamic lateral analysis to ensure stability and sufficient damping of the rotor.
- Rotordynamic torsional analysis.
- The bolted connection of the delivery cover to ensure tightness and to obtain the bolt and cover stresses and deformations.
- The interstage crossover to determine the stresses and deformations.
- The suction casing to ensure tightness and obtain the stresses.
- The suction nozzle and barrel to determine the opening compensation.
- The center and throttle sleeve to obtain stresses and deformations.
- Different stage casings and wear rings to determine their stresses and deformations.
- The DE bearing housing to obtain the natural frequencies.
- The NDE bearing housing to obtain its natural frequencies.
- The diffuser to determine its stresses and deformations.

Different programs were used for the analyses:

- A lateral software program was used for the lateral rotordynamics.
- A torsional software program was used for the torsional rotordynamics.
- An engineering simulation software was used for the structural finite element analyses of the other parts and assemblies.

The lateral and torsional software programs are inhouse codes, especially developed for the design of pumps, whereas the engineering simulation software is a general-purpose finite element code.

Design and analysis were closely working together to optimize the design. Modifications were derived from the analysis results and counterchecked by the analysis again. Special attention was paid to the models of the cover and the suction casing. The following sections describe the most interesting analyses.

Delivery Cover

By a finite element stress analysis, the stresses and deformations of the cover, the barrel, the connecting bolt, and the nut had to be computed and verified against allowable limits. The main objectives were the determination of the bolt stresses and its performance under loading conditions as well as the determination of the contact pressure between barrel and cover to ensure tightness.

A 3-D solid model had to be used for investigation. It was modeled within the finite element (FE) general-purpose code used for this analysis. Figure 14 shows the model. The barrel is cut at the right edge and axially fixed. Due to the 12 bolts, a 15 degree slice of the circumference was modeled. Symmetry conditions were used at the slice areas. Eight-noded brick elements were used to model the different parts. These were connected by nodal coupling in the direction of the acting forces where contact was ensured, or by contact elements, allowing contact or separation depending on the deformations. The four load cases of Table 5 were analyzed. The load cases 2 to 4 are superimposed over the preloading first load case.

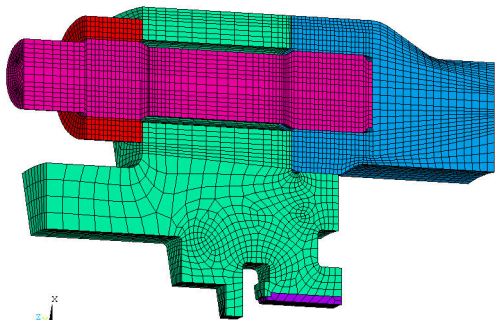

Figure 14. FE-Model of Cover and Bolted Connection with Barrel—Symmetry Is Used and 1/24th of Circumference Is Modeled.

Table 5. Load Cases Cover Analysis.

Load Case No.	Description	6th stage Pressure, p_1	Suction Pressure, p_2	Stage Casing Force, F_{SC}	Main Bolt Preload, F_{B1}	Mech. Seal Flange Load, F_{B2}
		[bar], (PSI)	[bar], (PSI)	[N], (lb)	[N], (lb)	[N], (lb)
1	Bolt Preload	0	0	0	$3.46*10^6$ ($7.63*10^6$)	0
2	Operation	384 (5570)	32 (465)	194,083 (427,872)		60,120 (132,540)
3	Design	736 (10,676)	736 (10,676)	0		$1.38*10^6$ ($3.04*10^6$)
4	Hydrotest	957 (13,880)	957 (13,880)	0		$2.92*10^6$ ($6.44*10^6$)

Figure 15 shows the qualitative deflection of the model at load case design. The interference between cover and barrel is due to the exaggeration. It seems that there is nearly no bending on the bolt. This is proven by Figure 16, showing the bolt stresses at the hydrotest load case. Obviously there is only a small bending moment on the bolt. The bolt loading is very static; the pressure loading of the structure reduces the contact load between barrel and cover, as Figure 17 shows. Figure 18 shows the forces of the contact elements for the hydrotest load case. Figure 19 shows the pressure of metal-to-metal contact. For the load cases' operation and design, the mean contact pressure is higher than the discharge pressure; for the load case hydrotest it is a little bit lower. Examination of its local dependency shows that in the inner regions the pressure is higher than the discharge pressure.

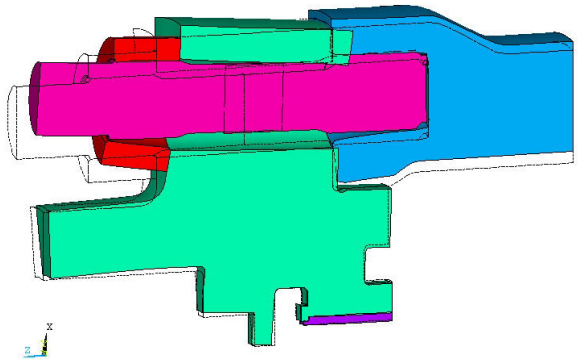

Figure 15. Deformations of Bolted Cover Connection for Load Case Design.

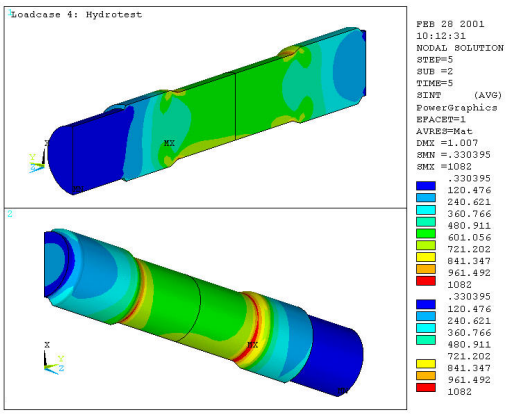

Figure 16. Tresca Bolt Stresses of Cover Connection at Load Case Hydrotest.

Figures 20 and 21 show the stresses of the barrel and the cover for the design load case. There is some edge pressure at the boreholes and some notch stresses, i.e., in the cover radius toward the sleeve of the mechanical seal, but in general the stresses are quite low. Evaluating the primary stresses of the barrel shows that the ASME limits are met and the notch stress of the cover is below the ASME limit for 10,000 cycles.

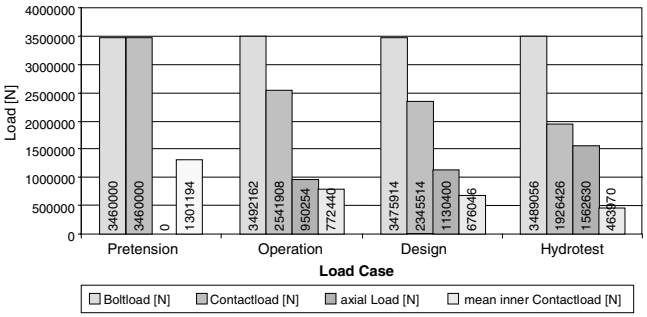

Figure 17. Bolt and Flange Loads of Cover Connection for Different Load Cases.

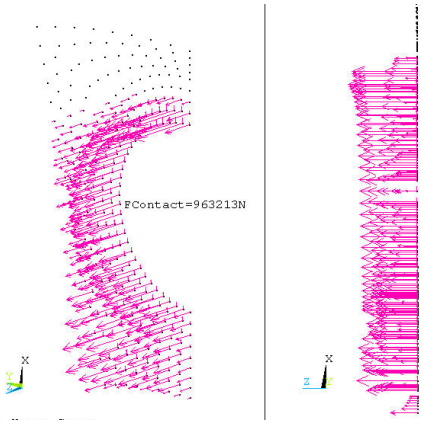

Figure 18. Nodal Contact Forces at Cover Flange for Load Case Hydrotest.

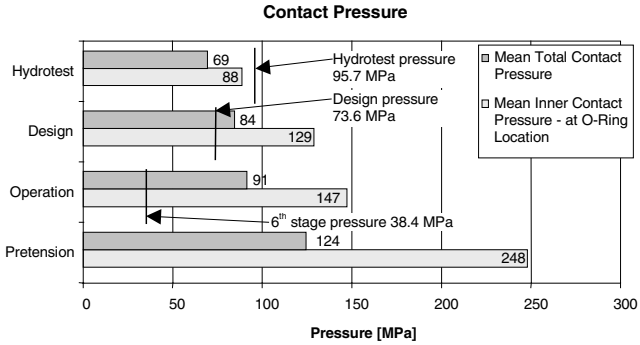

Figure 19. Cover Flange Contact Pressures for Different Load Cases.

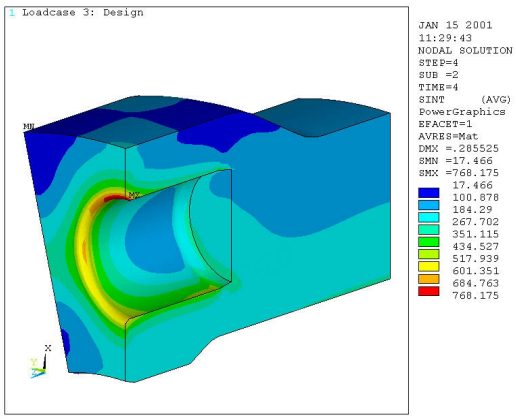

Figure 20. Equivalent Tresca Stresses of Barrel at Load Case Design.

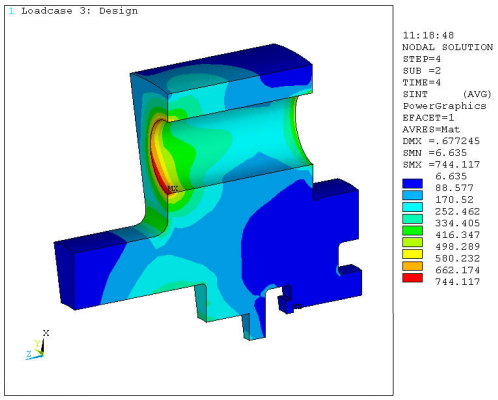

Figure 21. Equivalent Tresca Stresses of Cover at Load Case Design.

Suction Casing

With a finite element stress analysis, the stresses and deformations of the suction casing and the barrel were computed. The main objectives were the determination of the suction casing stresses and their performance under loading conditions as well as the determination of the radial gap between both parts in the region of the seal to ensure tightness.

A 3-D solid model had to be used for investigation. It was built within the 3-D computer-aided design (CAD)-modeler and transferred to the engineering simulation software, the FE general-purpose code used for this analysis. Within the engineering simulation software the mesh was created, loadings were established, and the material model was defined. Figure 22 shows the model. The barrel was cut at the right edge and axially fixed. Due to the eight ribs, a 22.5 degree slice of the circumference was modeled. Symmetry conditions were used at the slice areas. Ten-noded tetrahedron elements were used to model the two parts. Nodal coupling in the direction of the acting forces connected these parts at the common shoulder. Elastic-plastic material behavior with kinematic hardening, as shown in Figure 23, was used for the suction casing. This was selected due to the high stresses occurring in the shoulder under the notch. The five load cases of Table 6 were analyzed.

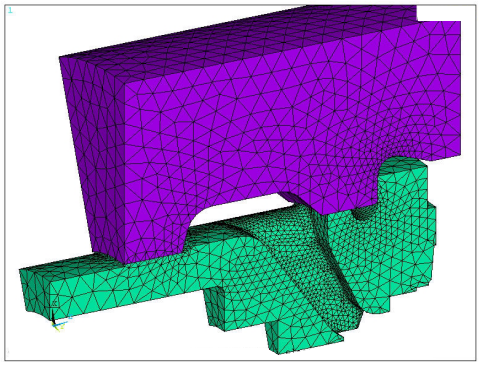

Figure 22. FE-Model of Suction Casing and Corresponding Part of Barrel—Symmetry Is Used and 1/16th of Circumference Is Modeled.

Due to the nonlinearity of the material, the sequence of load cases was essential. As the hydrotest was the first loading, it had to be computed first. Unloading the structure left residual stresses in the suction casing, upon which additional load cases were applied. The unloading load cases were computed obtaining the residual compressive stresses.

Figure 24 shows the qualitative distortion due to hydrotest pressure. There are large tensile strains at the notch below the shoulder. Figure 25 shows the stress-strain path of this location.

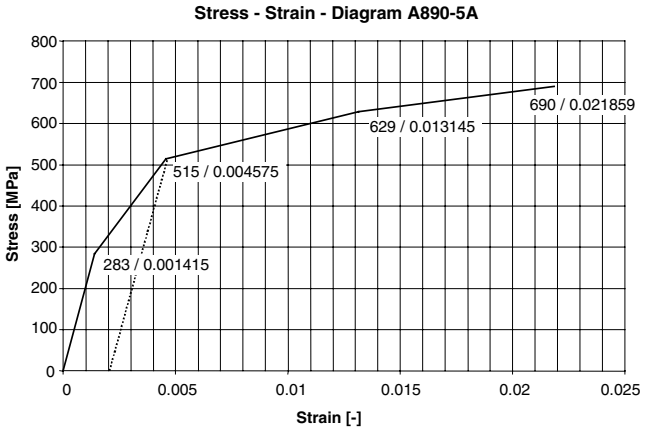

Figure 23. Stress Strain Relation of Suction Casing Material with Yield Stress of 515 MPa and Tensile Strength of 690 MPa.

Table 6. Load Cases Suction Casing Analysis.

Load Case No.	Description	Suction Pressure p_1	Discharge Pressure p_2	1st Stage Pressure p_3	Stage Casing Load, F_1	Mechanical Seal Flange Load, F_{B2}
		[bar] (PSI)	[bar] (PSI)	[bar] (PSI)	[N] (lb)	[N] (lb)
1	Hydrotest	957 (13,880)	957 (13,880)	957 (13,880)	0	$2.92*10^6$ ($6.48*10^6$)
2	Unload 1	0	0	0	0	0
3	Design	736 (10,676)	736 (10,676)	736 (10,676)	0	$1.38*10^6$ ($3.04*10^6$)
4	Unload 2	0	0	0	0	0
5	Operation	32 (465)	736 (10,676)	91 (1320)	$4.66*10^6$ ($10.3*10^6$)	60,120 (132,540)

During hydrotest, the stresses go up until point 3. Unloading leaves compressive residual stresses of about -200 N/mm^2 (-29 ksi), point 4. Succeeding operational loading leaves the stresses at this location to be of compressive nature, point 6. The stress range is purely linear.

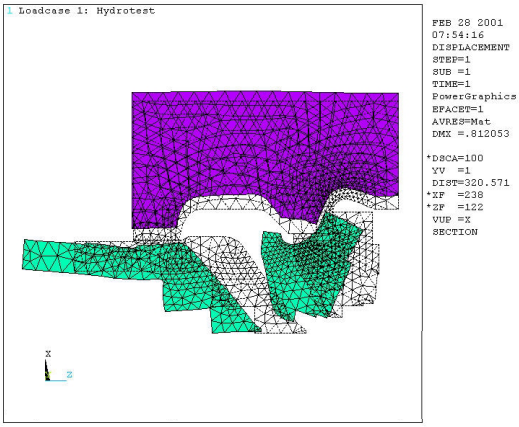

Figure 24. Distortion of Suction Casing and Barrel at Load Case Hydrotest.

Material testing was performed to determine the influence of compressive residual stresses in notches on the fatigue of the A890 Gr 5 material (Figure 26). Notched test bars were prestressed to a local strain of 1.7 percent in the notch. The succeeding endurance test showed a significant increase of the fatigue limit compared to test bars that were not prestressed. As the fatigue limit is more than 200 N/mm^2 (29 ksi), and the stress range at the notch between no loading and operation is less than 200 N/mm^2 (29 ksi), the suction casing will withstand the loading.

The radial deformation is of interest to judge the tightness at the seal position between the suction casing and the barrel casing. Figure 27 shows the gap due to tolerance and loading for the

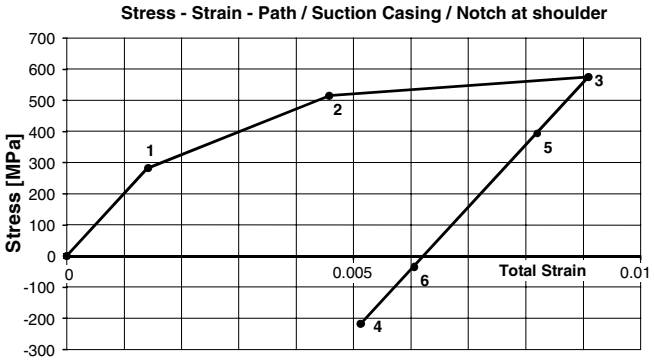

Figure 25. Stress-Strain Path at Shoulder Notch of Suction Casing—Loading from Point 0 to 3, Unloading to Point 4, Design and Operation at Points 5 and 6.

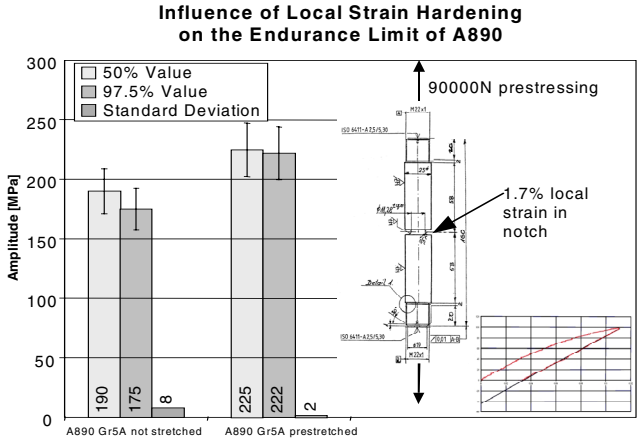

Figure 26. Endurance Limit Change Due to Local Plastic Prestressing of Suction Casing Material.

corresponding load cases. The seal has to be tight at the maximum radial gap of 0.326 mm (0.013 in) during hydrotest. This is possible due to the cold temperature, the slow creeping of the seal, and the short duration of the hydrotest. During normal operation, both pressure (32 bar [465 psi]) and gap (0.053 mm [0.0021 in]) are lower and the seal will be tight.

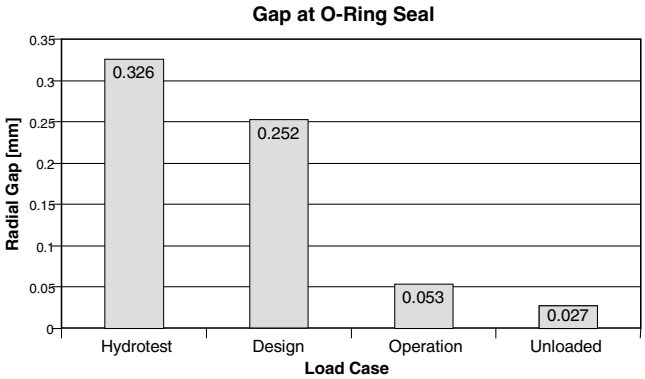

Figure 27. Radial Gap Sizes Between Suction Casing and Barrel at Different Load Cases.

Suction Branch and Barrel

The suction branch was analyzed by means of the finite element method to meet the requirements set in the ASME Code, Section VIII, Division 1, concerning the opening compensation. The finite element program for the analysis was one in which the model was built and meshed (Figure 28). Two load cases were analyzed, design (736 bar, 10,676 psi) and test condition (957 bar, 13,881 psi). Figure 29 shows the area of interest. This area 49 represents the available metal area for the nozzle opening. The effective nozzle wall length 2.5*t_n corresponds to UG37.1, and 3 mm (.012 inch) corrosion allowance was taken into account in the overhang length of the barrel. The sum of reaction forces of the nodes of this area divided by the area was compared with allowable nominal stresses of the duplex material A182 Gr F53, as shown in Table 7.

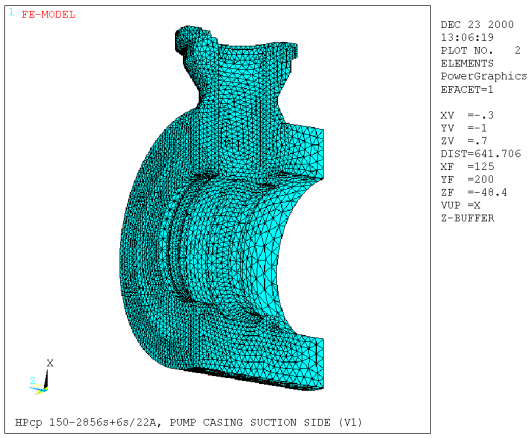

Figure 28. Analysis Model of Barrel End to Check Opening Compensation According to ASME Code.

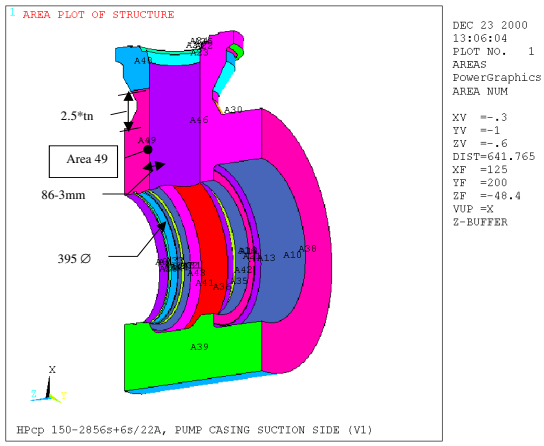

Figure 29. Area of Interest for Opening Compensation of Suction Nozzle.

Table 7. Area Compensation.

Condition	Operation	Test
Temperature [°C] (°F)	91 (196)	20 (68)
Yield Strength S_y [N/mm^2] (KSI)	458 (66.4)	515 (74.6)
Ultimate Strength S_u [N/mm^2] (KSI)	690 (100)	750 (109)
Allowable Membrane Stress [N/mm^2] (KSI) ❑ $S_m = S_u / 3.5$ for Design [ASME Code] ❑ $S_{all} = S_y / 1.3$ for Test [Designer Guideline]	197 (28.6)	396 (57.4)
Area Size # 49 [mm^2] (in^2)	22,545 (34.95)	
Area Force [N] (lb)	4.38 *10^6 (9.65*10^6)	5.75 *10^6 (12.7*10^6)
Nominal Membrane Stress [N/mm^2] (KSI)	195 (28.3)	255 (37.0)

The calculated values are below the limits. Additionally, the radial opening of the barrel at the O-ring position, sealing between barrel and suction casing, was evaluated (Figures 30 and 31). The values are nearly identical to those of the suction casing and barrel analysis.

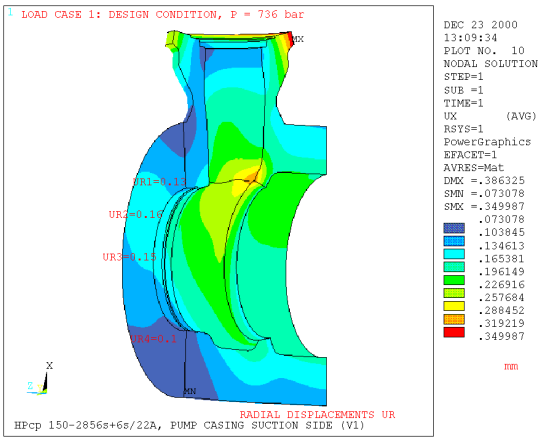

Figure 30. Radial Displacements of Barrel End at Design Conditions.

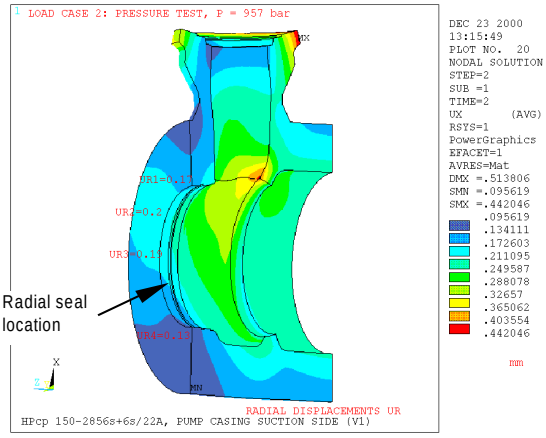

Figure 31. Radial Displacements of Barrel End at Test Conditions.

Stage Casings

The stage casings of the first set of impellers were subjected to the full discharge pressure at the outside and with the much smaller increasing stage pressure at the inside. Due to the external loading, a reduction of the running clearance during operation was anticipated. A loose fit between the wear ring and the stage casing at assembly was selected, which changes to a press fit during operation. Axis-symmetric engineering simulation software models were made for the second and the fifth stage casing. The flanged wear ring design with its loose fit between the wear ring and the stage casing was modeled (Figure 32). The resulting radial reduction of the running clearance at operation is within acceptable limits (Figure 33). The maximum radial compression at the wear ring/stage casing fit was 0.061 mm (.002 inch). The maximum stresses show a high peak at the O-ring groove, but with $\sigma_{v,\,max}$ = 302 N/mm^2 (43.8 ksi), this value is acceptable. The stresses were much lower everywhere else in the part.

ROTORDYNAMICS

The rotordynamic behavior of pumps depends on the mechanical design of the rotor, the fluid forces developed in the close running clearances, the interaction between impellers and diffusers, and the dynamic properties of the bearings. Hydraulic components, labyrinth seal configurations, and swirl breaks have been applied, following design guidelines established during the EPRI Research Program (1993) and as further developed over the past years.

Damped Lateral Critical Speeds Analysis

Lateral critical speeds occur at the intersection points between the speed dependant eigenfrequency curves and the synchronous

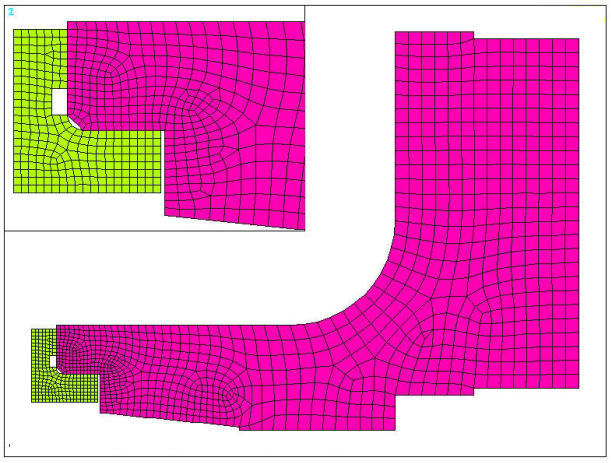

Figure 32 Axisymmetric Analysis Model of Stage Casing and Wear Ring #2.

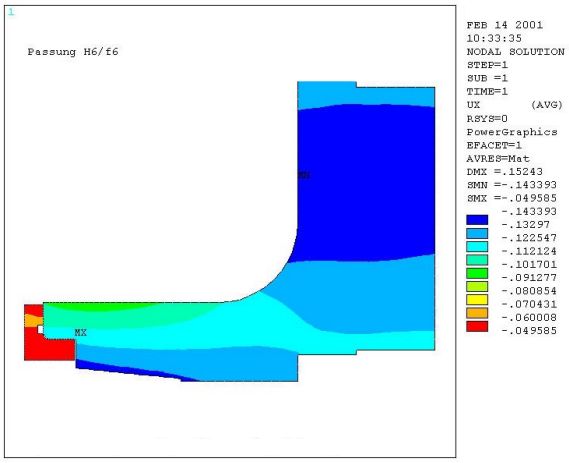

Figure 33. Radial Deflections of Stage Casing and Wear Ring under External and Internal Pressure.

excitation line. For each critical speed the corresponding modal damping is calculated.

The rotor model (Figure 34) accounts for the stiffness and mass of the shaft. Shaft seals and impellers are added as distributed additional mass effects and have no influence on the overall stiffness. Speed dependant boundary conditions are applied at bearing, annular seal, and center bushing and throttle bushing locations to model the interaction forces.

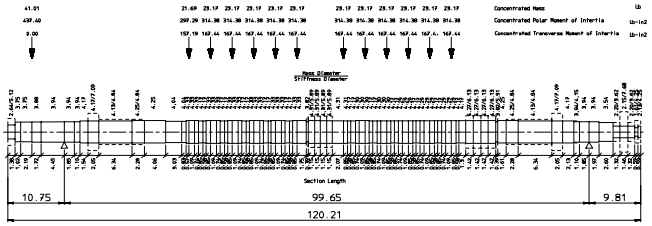

Figure 34. Rotor Model.

The behavior of the rotor results from the interaction between the shaft, the forces acting on it, and the supporting influences provided by the stiffness and damping levels at the bearings, annular seals, center bushing, and throttle bushing. These factors vary with speed, load, and the level of seal wear. Stiffness and damping magnitudes of bearings, annular seals, center bushing, and throttle bushing are considered by the program to be speed dependant.

For standstill the rotor is centered in the center bore of the casing at the mechanical seal location and rests in the center bushing. The bearings are radially loaded by the rotor mass. The resulting bearing vertical upward lift guarantees optimum bearing setting with respect to bearing load and rotordynamic behavior (Table 8).

Table 8. Rotor Setting and Bearing Loads, European Definition of Sommerfeld-Number.

Load case	Bearing vertical upward lift at DE and NDE		Non-dimensional static bearing load expressed by Sommerfeld-Number	
	e_{DE}	e_{NDE}	So_{DE} [--]	So_{NDE} [--]
@ 6000 rpm	0.176 mm (0.00693 in)	0.183 mm (0.00720 in)	0.03663	0.05141

With a nonlinear static analysis, the static load of the bearings and the static rotor deflection have been evaluated at rated speed condition for the defined bearing vertical upward lift (Figure 35).

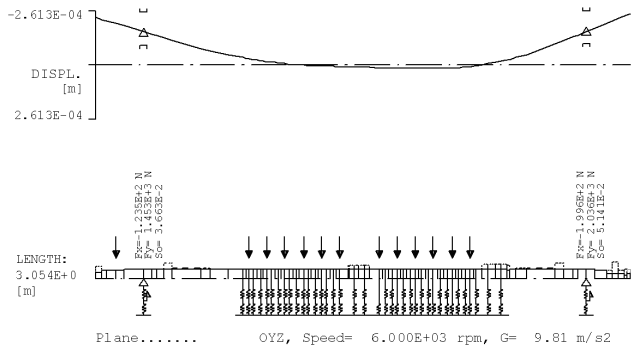

Figure 35. Nonlinear Static Analysis.

The inhouse lateral software computer code, which is especially designed for pump lateral rotordynamic analysis, has been used to carry out these calculations. The core of this program is the finite element-based computer code especially designed for rotordynamic calculations. Seal coefficients are calculated by a computer code based on the theory developed by Florjancic (1990). Stiffness and damping coefficients of the hydrodynamic four-lobe bearings are obtained from the analysis with a computer code for calculation of bearing coefficients.

Eigenvectors are plotted in an isometric view and are represented by solid lines. The undeformed rotor has chain dot representation. When estimating local amplitudes and considering the rotor modal deformation as a spatial view projected into one plane, vibration amplitudes, shown as orbits, can be drawn at locations of interest. Vibration orbits are drawn as dotted lines at the location of maximum amplitude and as solid lines at the other shown locations. Damping values are expressed as "damping coefficient," D.

The pump-rotor at *new*-condition (design clearances) (Figures 36 and 37) and *worn*-condition (2× design clearances) (Figures 38 and 39) have been investigated for pump data at operating condition.

Under *new*- and *worn*-conditions, the first eigenmode is dominated by higher vibration amplitudes within the annular seals, mainly of the first six stages, and at the coupling. The use of swirl brakes at the annular suction side seals of the first six stages produces high damping, which decreases with increasing speed and seal wear. In both cases no critical speed was detected for a speed range up to 8000 rpm.

Eigenmodes with a modal damping > 40 percent over the full speed range, as well as eigenmodes outside a frequency range from zero to 2.2 times maximum continuous speed, are not shown. The modal damping levels at the investigated rotor-speeds are compared to minimum required damping levels according to API 610 Eighth Edition (1995) (Figure 40).

The analysis indicates that the pump fulfills the damping requirements of API 610 Eighth Edition (1995) for the relevant eigenmodes under *new*- and *worn*-conditions.

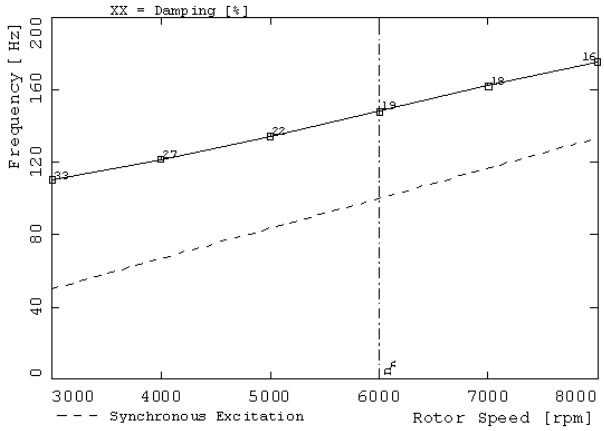

Figure 36. Campbell Diagram, New-Condition.

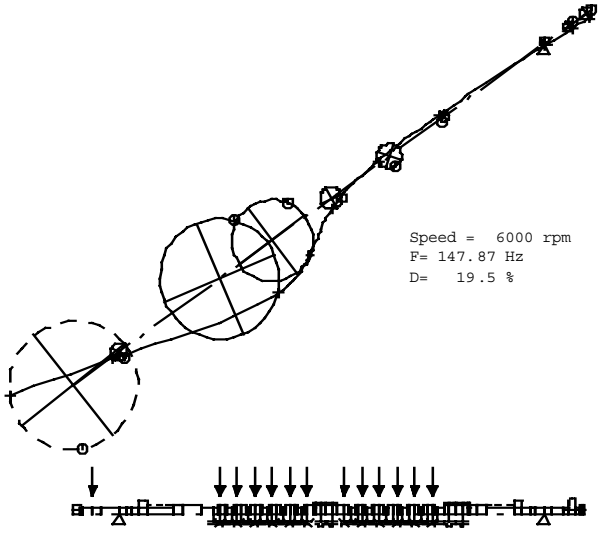

Figure 37. First Bending Mode, New-Condition.

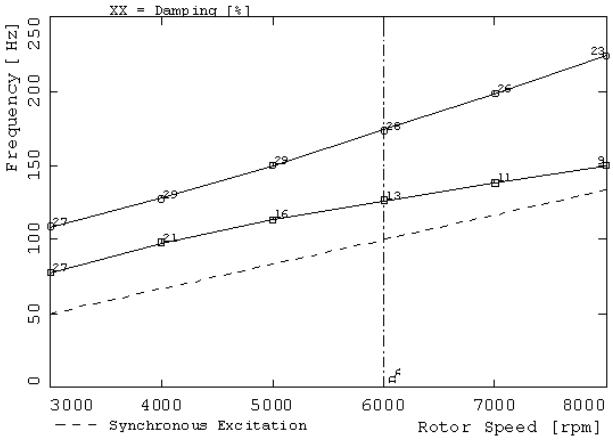

Figure 38. Campbell Diagram, Worn-Condition.

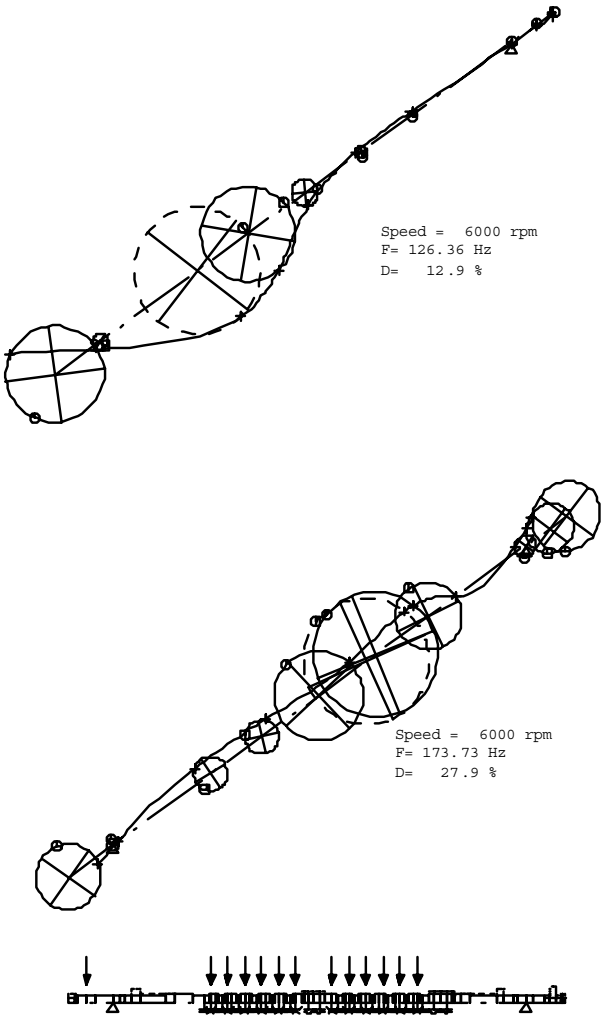

Figure 39. First and Second Bending Mode, Worn-Condition.

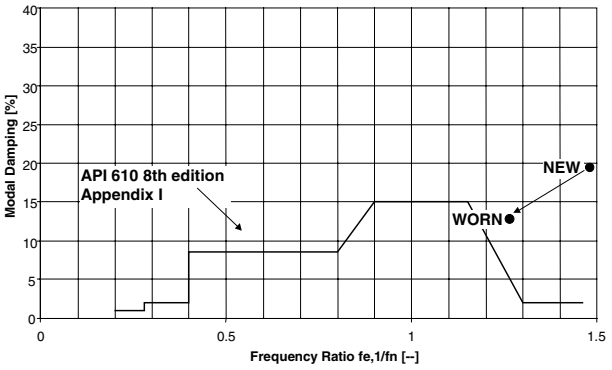

Figure 40. Evolution of First Eigenmode from New- to Worn-Condition.

Damped Coupling Sensitivity Analysis

To estimate the effect of mechanical unbalance, a linear harmonic response analysis, applying unbalance mass at coupling location, was carried out for both clearances. Pump rotors should be as insensitive to unbalance as possible. In order to ensure this criterion during design stage, a dimensionless coupling unbalance sensitivity factor is defined using the following formula and judged against calculations and measurements on many different machines, that is to an "experience" base (Bolleter, et al., 1990).

$$SF = \left(Y / U\right) * m \tag{2}$$

where:

SF = Coupling sensitivity factor
Y = Major semiaxis of vibration orbit at the coupling center of gravity location
U = Unbalance (of arbitrary magnitude) placed at the coupling center of gravity location
m = Rotor mass = 404.2 kg (891.11 lb)

The results of the coupling sensitivity analysis for the described rotor are given in Table 9 (Figure 41 and 42). For illustration, an unbalance force of one-fourth of the rotor weight as specified by the feedpump guidelines would then result in the calculated amplitudes at the coupling.

Table 9. Results of Coupling Sensitivity Analysis.

Load case	Coupling Sensitivity Factor, SF [--]	Coupling Unbalance = ¼ Rotor Weight, U [*E-06 m kg]	Major semi axis of vibration orbit at the coupling center of gravity location, Y [mm]
6000 rpm / NEW	4.847	2515.0 (0.2184 lb in)	0.030 (0.00118 in)
6000 rpm / WORN	4.988	2515.0 (0.2184 lb in)	0.031 (0.00122 in)

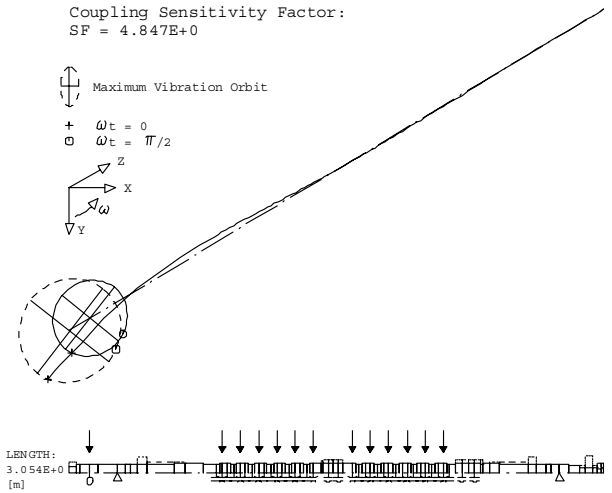

Figure 41. Coupling Sensitivity at 6000 RPM, New-Condition.

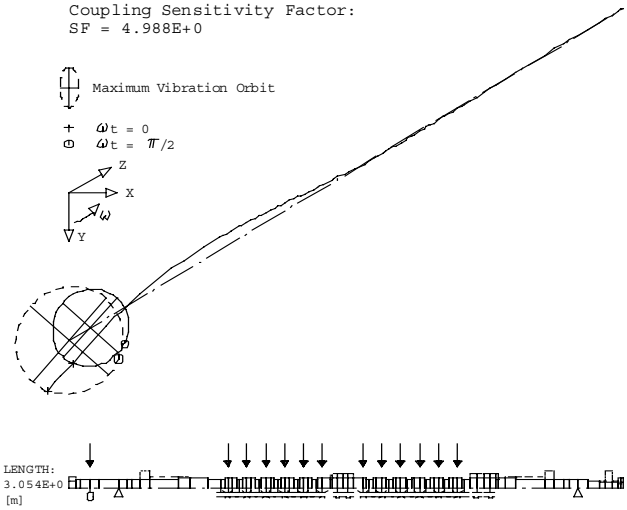

Figure 42. Coupling Sensitivity at 6000 RPM, Worn-Condition.

No coupling unbalance sensitivity factor (SF) of the rotor system is greater than five. The history of successful machines in operation shows that no vibration problems due to mechanical unbalance at the coupling are to be expected with a sensitivity factor SF <12.0.

Comparison of Results with Proprietary Rotordynamic Code

The lateral rotordynamic analysis for this project was verified by the client using a proprietary rotordynamic code and its commercial equivalent. The mechanical rotor model, mass and stiffness diameters, mass points, and inertia, was prepared in the main program, based on the shaft sections defined within the lateral software program. A first run, obtaining the natural frequencies in air of the rotor supported by rigid bearings has shown coincidence in frequencies and mode shapes.

When calculating the damped eigenfrequencies, the following modules were verified and results compared.

Calculating Annular Seal Coefficients

For annular seals with preswirl at seal inlet around 0.5 (making use of swirl breaks), all rotordynamic coefficients have shown good coincidence. The input of relative roughness on stator and rotor plays an important role, changing $\text{Reynolds}_{\text{axial}}$ and influencing direct stiffness dramatically.

Calculating Impeller Interaction Coefficients

Coefficients are based on published results from measurements at 160°C (320°F) from EPRI TR-100980 (1992). No correction for different specific speeds, as done within the lateral software program, will be performed.

Calculating Journal Bearing Coefficients

A comparison with the bearing coefficient calculation software and DIN 31657 (1996) has shown good coincidence in the rotordynamic coefficients calculated versus eccentricity.

A damped eigenmode calculation, as well as a forced response calculation were performed with the proprietary rotordynamic code. The first eigenmodes and their modal damping correspond within 5 percent of the prediction by the lateral software program. The mode shapes show the same behavior (Figures 43 and 44). Also for the forced response, good correspondence for maximum amplitudes could be obtained. Location of maximum amplitudes was identical.

This good correspondence could be achieved due to the fact that the main contribution comes from the impeller suction side annular seals having swirl breaks, for which good correspondence in rotordynamic coefficients could be found.

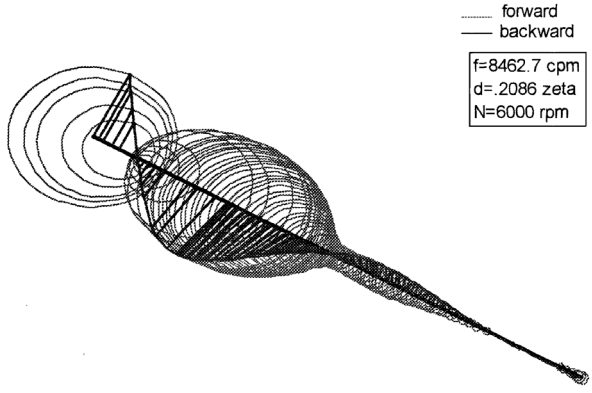

Figure 43. Damped Eigenvalue Mode Shape Plot, New-Condition.

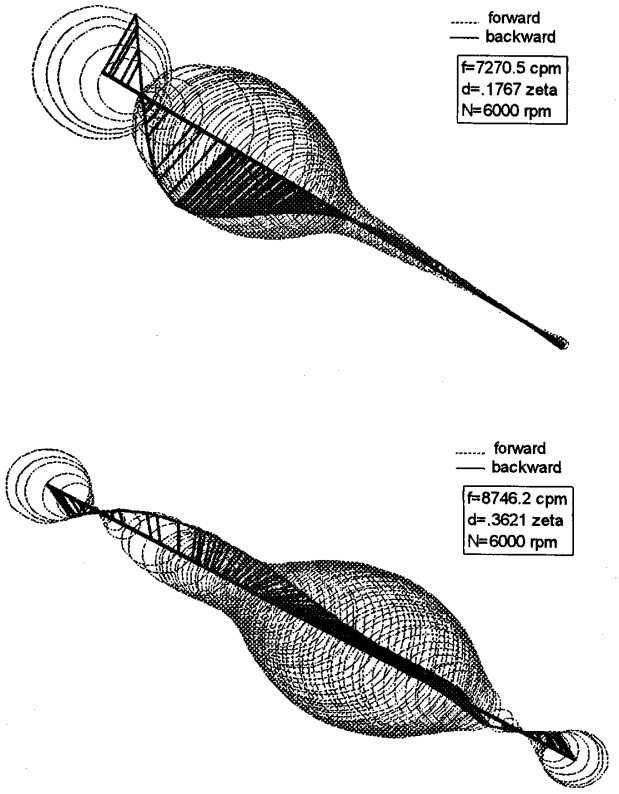

Figure 44. Damped Eigenvalue Mode Shape Plot, Worn-Condition.

PROTOTYPE TEST

Evaluation of Calculation Results by Rotordynamic Tests

Rotor Tap Test

The rotor was assembled in its final running condition (except for mechanical seal sleeves and bearing housing oil seals) and supported in Vee-blocks on a level inspection table at the bearing journal locations. An accelerometer with the weight of 37 g (0.0816 lb) was attached to the underside of the center sleeve in the vertical plane using mounting wax. The rotor was tapped gently in the center of the span with a soft mallet in the downward vertical direction. The response from the accelerometer was displayed on a spectrum analyzer. Figure 45 shows one of the resonance spectra of the tap test.

A comparison with the calculated eigenfrequencies in air by the lateral software program is presented in Table 10 (Figure 46). Calculated rotor eigenfrequencies in air correspond within 7 percent of the measured ones from the tap test.

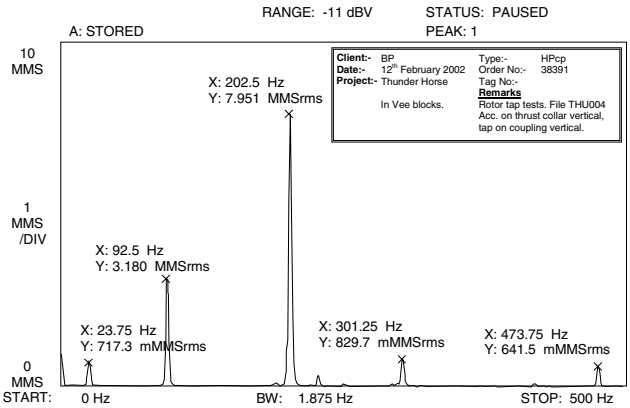

Figure 45. Resonance Spectrum of Rotor Tap Test.

Table 10. Comparison of Results from Rotor Tap Test.

Test No.	3 (Vee-blocks)	4 (Vee-blocks)	5 (Vee-blocks)	Calculated
Tap on:	centre sleeve	coupling vertical	center sleeve	--
Measured at:	centre sleeve	thrust collar	coupling	--
1st Eigenmode	23.75 Hz	23.75 Hz	23.75 Hz	22.25 Hz
2nd Eigenmode	92.50 Hz	92.50 Hz		90.75 Hz
3rd Eigenmode	201.25 Hz	202.50 Hz	202.50 Hz	201.44 Hz
4th Eigenmode		301.25 Hz		307.78 Hz

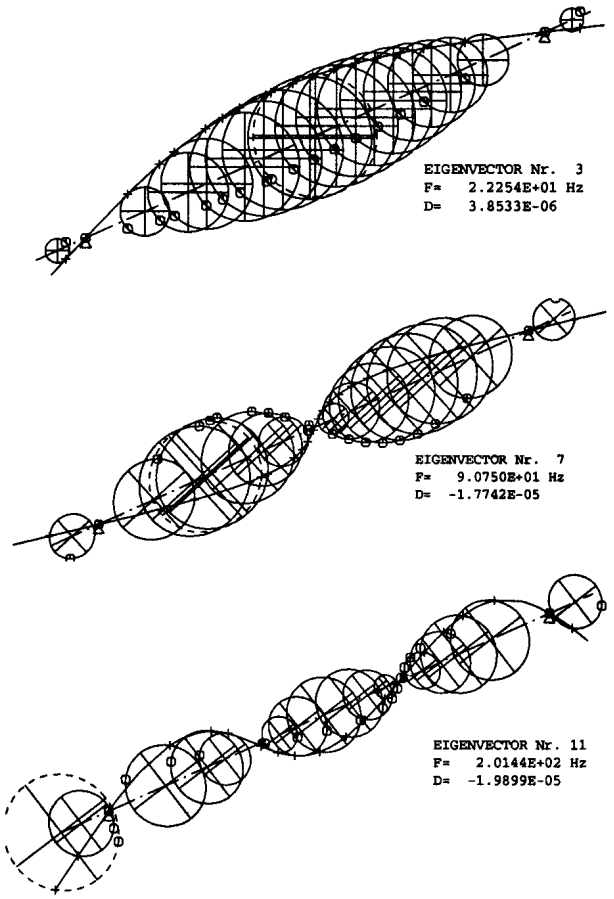

Figure 46. Calculated Eigenmodes in Air.

1× and 2× Design Clearance Acceptance Test

The pump was run up to full speed of 6000 rpm at different flow points. Vibration characteristics at these flow points were obtained under steady-state condition. Additionally, the vibration characteristic of certain flow points at reduced speed was recorded.

This test was done for 1× design clearances and 2× design clearances. Frequency spectrum plots of the pump for 1× and 2×, respectively, design clearance are shown in Figures 47 and 48 for nominal speed and rated flow condition. Additionally, the overall vibration levels for other speed-flow conditions are summarized in Table 11.

The spectrum plots show no sign of resonance amplification or vibrations at blade passage frequency, nor could a sign of instability be observed at enlarged clearances.

The peak at 2× speed frequency in the spectrum plot for design clearance condition indicates a slight misalignment, explaining the slightly increased vibration readings under this condition.

The unfiltered peak-to-peak vibration amplitude at the journal bearing should not exceed one-third of the diametral bearing clearance. A maximum of 23 percent utilization of the diametral bearing clearance when running under 2× clearance condition could be observed.

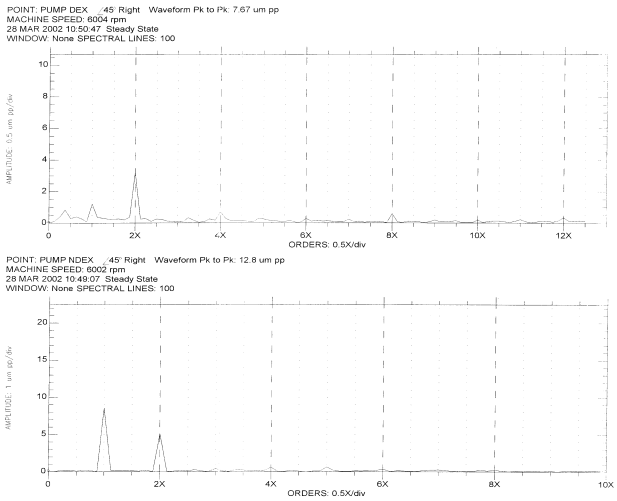

Figure 47. Frequency Spectrum at 6000 RPM and 331 M^3/H (1457 GPM) Rated Flow, New-Condition.

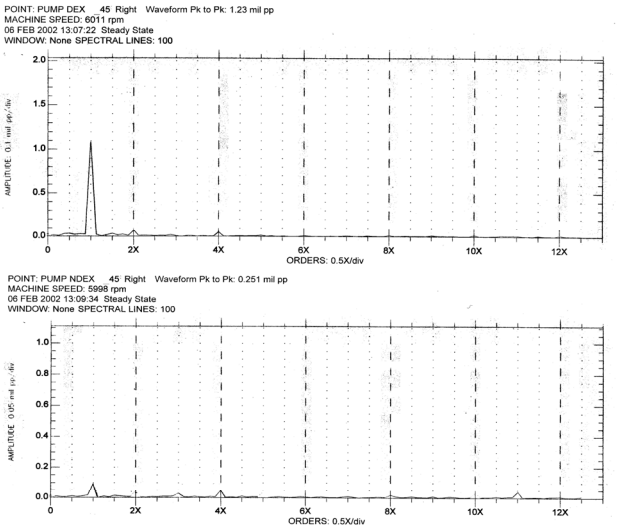

Figure 48. Frequency Spectrum at 6000 RPM and 332 M^3/H (1462 GPM) Rated Flow, Worn-Condition.

Table 11. Overall Vibration Levels at DE and NDE.

1x Design Clearance

Speed [rpm]	Flow [% BEP]	DE-X (45°) peak-peak	DE-Y (45°) peak-peak	DE-Vertical RMS	DE-Horizontal RMS	NDE-X (45°) peak-peak	NDE-Y (45°) peak-peak	NDE-Vertical RMS	NDE-Horizontal RMS
6000	60	6.35 µm (0.25 mil)	7.11 µm (0.28 mil)	2.24 mm/s (0.088 in/s)	2.56 mm/s (0.101 in/s)	9.40 µm (0.37 mil)	9.40 µm (0.37 mil)	1.35 mm/s (0.053 in/s)	1.68 mm/s (0.066 in/s)

2x Design Clearance

Speed [rpm]	Flow [% BEP]	DE-X (45°) peak-peak	DE-Y (45°) peak-peak	DE-Vertical RMS	DE-Horizontal RMS	NDE-X (45°) peak-peak	NDE-Y (45°) peak-peak	NDE-Vertical RMS	NDE-Horizontal RMS
5400	20	25.91 µm (1.02 mil)	26.16 µm (1.03 mil)	1.42 mm/s (0.056 in/s)	0.94 mm/s (0.037 in/s)	5.33 µm (0.21 mil)	5.33 µm (0.21 mil)	0.69 mm/s (0.027 in/s)	0.53 mm/s (0.021 in/s)
	60	21.08 µm (0.83 mil)	20.32 µm (0.80 mil)	0.96 mm/s (0.038 in/s)	0.69 mm/s (0.027 in/s)	4.83 µm (0.19 mil)	4.32 µm (0.17 mil)	0.48 mm/s (0.019 in/s)	0.48 mm/s (0.019 in/s)
	100	21.34 µm (0.84 mil)	20.07 µm (0.79 mil)	1.17 mm/s (0.046 in/s)	0.94 mm/s (0.037 in/s)	5.59 µm (0.22 mil)	5.59 µm (0.22 mil)	0.46 mm/s (0.018 in/s)	0.48 mm/s (0.019 in/s)
5820	95	22.61 µm (0.89 mil)	21.84 µm (0.86 mil)	0.89 mm/s (0.035 in/s)	0.58 mm/s (0.023 in/s)	5.33 µm (0.21 mil)	5.33 µm (0.21 mil)	0.43 mm/s (0.017 in/s)	0.53 mm/s (0.021 in/s)
6000	20	29.72 µm (1.17 mil)	29.46 µm (1.16 mil)	1.65 mm/s (0.065 in/s)	1.09 mm/s (0.043 in/s)	5.84 µm (0.23 mil)	5.59 µm (0.22 mil)	0.76 mm/s (0.030 in/s)	0.69 mm/s (0.027 in/s)
	50	23.11 µm (0.91 mil)	22.35 µm (0.88 mil)	1.17 mm/s (0.046 in/s)	0.94 mm/s (0.037 in/s)	4.57 µm (0.18 mil)	4.06 µm (0.16 mil)	0.48 mm/s (0.019 in/s)	0.53 mm/s (0.021 in/s)
	60	22.86 µm (0.90 mil)	22.35 µm (0.88 mil)	1.19 mm/s (0.047 in/s)	0.89 mm/s (0.035 in/s)	4.32 µm (0.17 mil)	4.06 µm (0.16 mil)	0.46 mm/s (0.018 in/s)	0.53 mm/s (0.021 in/s)
	75	24.13 µm (0.95 mil)	22.86 µm (0.90 mil)	0.94 mm/s (0.037 in/s)	0.58 mm/s (0.023 in/s)	4.32 µm (0.17 mil)	3.81 µm (0.15 mil)	0.43 mm/s (0.017 in/s)	0.51 mm/s (0.020 in/s)
	95	23.37 µm (0.92 mil)	22.61 µm (0.89 mil)	1.04 mm/s (0.041 in/s)	0.53 mm/s (0.021 in/s)	4.83 µm (0.19 mil)	5.08 µm (0.20 mil)	0.51 mm/s (0.020 in/s)	0.53 mm/s (0.021 in/s)
	100	23.88 µm (0.94 mil)	22.86 µm (0.90 mil)	1.50 mm/s (0.059 in/s)	0.84 mm/s (0.033 in/s)	5.33 µm (0.21 mil)	5.33 µm (0.21 mil)	0.53 mm/s (0.021 in/s)	0.53 mm/s (0.021 in/s)

API 610, Eighth Edition (1995), limits the maximum unfiltered vibration velocity at bearing housings at below 3.0 mm/s (0.12 in/s) root-mean-square (RMS) and the maximum unfiltered pump shaft displacement at below 29.44 µm (1.16 mils) peak-to-peak for the pump during performance test (1× design clearance). These API 610 (1995) requirements are fulfilled, even for end of life (2× design clearance) condition.

Coupling Unbalance Test

The test procedure follows basically API 610, Eighth Edition (1995), Appendix I. First the pump was run up to full speed of 5997 rpm at duty flow to obtain the basic vibration characteristics and record the rundown. Then a trial weight was added at the unbalance plane in line with the maximum vector, and the vibration characteristic was assessed as in the first step. In the following run the trial weight was adjusted to cause the maximum vector at the bearing to increase by 150 to 200 percent. The results and the rundown were recorded in order to determine if a critical response was present. Since the "as-built" rotor (Figure 49) contains both residual mechanical as well as considerable hydraulic unbalance, which add to the effect of the trial unbalances, dismantling the pump is not allowed when the additional unbalances are fitted. This guarantees the residual unbalance condition did not change between the runs.

The test was performed for 2× design clearance condition only. Unbalance sensitivity was to be expected at the drive-end based on the mode shape plots of the eigenanalysis. Therefore, the trial unbalance masses were attached to the coupling disk (Figure 50).

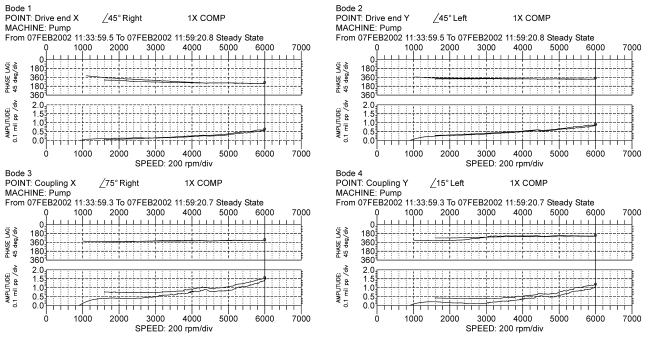

Figure 49. Rotor "As-Built" (G 2.5).

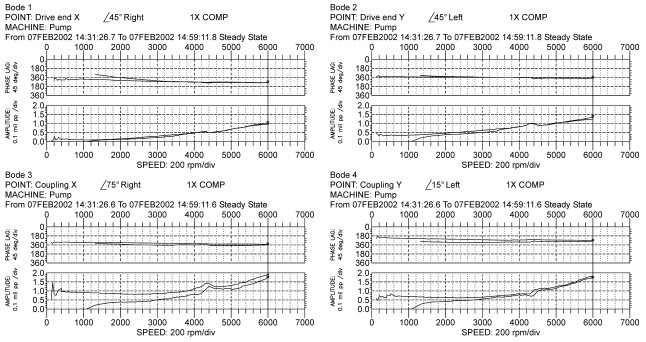

Figure 50. Trial Balanced Rotor (G 10).

The definition of the unbalance follows ISO 1940-1 (1986):

$$U = G*60*1000*m/\left(2*\pi*n\right) \qquad (3)$$

where:

U = Unbalance in kg m
G = ISO balance grade in mm/s
n = Rotor speed in rpm
m = Rotor mass = 404.2 kg (891.11 lb)

The results are compared to the predicted unbalance response calculated with the lateral computer software.

Since the calculation starts from a perfectly balanced system, the vector difference of the response between the "as-built" rotor (G 2.5) and the trial-balanced rotor (G 10) from the test can only be compared (Figure 51). The unbalance difference ΔU of 4.83E-03 kg m (0.419 lb in) was used for the calculated unbalance response and applied at the coupling (Figure 52, Table 12).

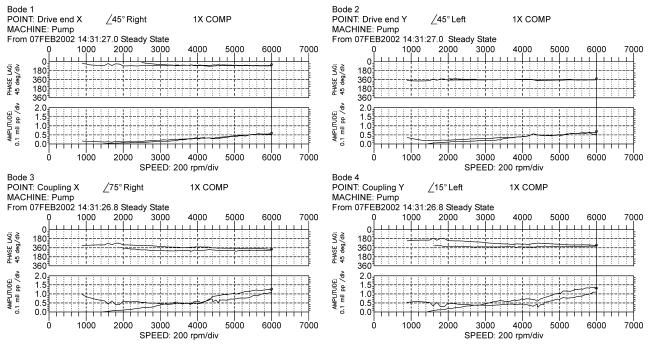

Figure 51. Vector Difference Due to Added Trial Balance Mass.

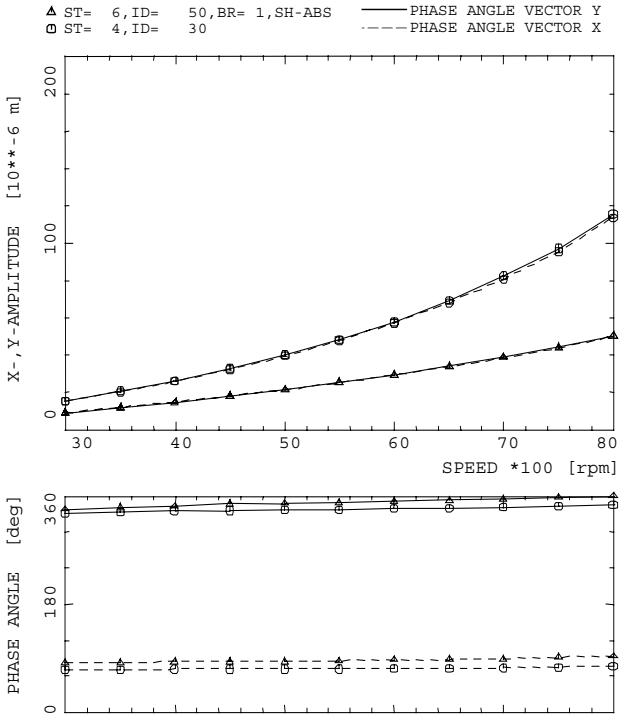

Figure 52. Unbalance Response ΔU = 4.83E-03 Kg M (0.419 Lb In), (ID50 = DE-Bearing, ID30 = Coupling).

Table 12. Comparison of Vibration Amplitudes for ΔU = 4.83 E-03 Kg M (0.419 Lb In).

Load case: ***6000 rpm / 2x Design Clearance***	**Major semi axis of vibration orbit** ***Calculation***	**Major semi axis of vibration orbit** ***Test***
DE-Bearing	0.030 mm (1.18 mils)	0.008 mm (0.32 mils)
Coupling	0.058 mm (2.28 mils)	0.016 mm (0.63 mils)
Coupling Sensitivity Factor, SF according equation (2)	4.85	1.34

The correspondence of responses between test and prediction is poor, but the prediction calculation is on the "safe" side since the measured response amplitudes are far below the predicted ones. Previous unbalance tests for other projects (Frei, et al., 1990) have shown the same discrepancies. The reason for this behavior is the strong dependence of the bearing rotordynamic coefficients on static load because the coupling overhung mode is mainly determined by the DE-bearing characteristics. Slight differences in influencing parameters such as:

- Rotor setting (bearing vertical upward lift)

- Viscosity and temperature of lubricant oil
- Geometric tolerances in bearing clearance
- Preload of the four-lobe bearing

cause big discrepancies in the response results.

On the other hand, amplitudes are generally small and the relative error from measurement as well as from vector difference procedure are therefore large.

The test confirmed the absence of any critical speed within the operating speed range and shows that the pump is insensitive to the applied coupling unbalance. The pump rotor still has heavy damping at 2× clearance condition, which is confirmed by the analytical results.

Hydrostatic Pressure Test

The hydrostatic pressure test assembly, as shown in Figure 53, was installed in a pit for safety reasons. Fluorescent dye had been added to the test water and ultraviolet lamps were set up to facilitate visual leakage detection with four video recording cameras. Pressure transmitters were added at the location of the "telltale" leakage detection connections, in addition, to indicate any leakage at the suction cover and delivery cover joints. No personnel were allowed near the test assembly during the test for safety reasons. The pressure was incrementally raised up to 500 bar (7252 psi) and held for 30 minutes. After that, the pressure was again incrementally raised up to the end pressure of 957 bar (13,880 psi) and held for another 30 minutes. No leakage was detected and the hydrostatic end pressure could be maintained at the duration of the test. The barrel casing bores at the locations of the suction casing and the interstage crossover were measured prior to the test and compared to the dimensions measured after the strip down. The deviations were within the measuring tolerances, e.g., hardly any deformation resulted from the hydrostatic pressure test.

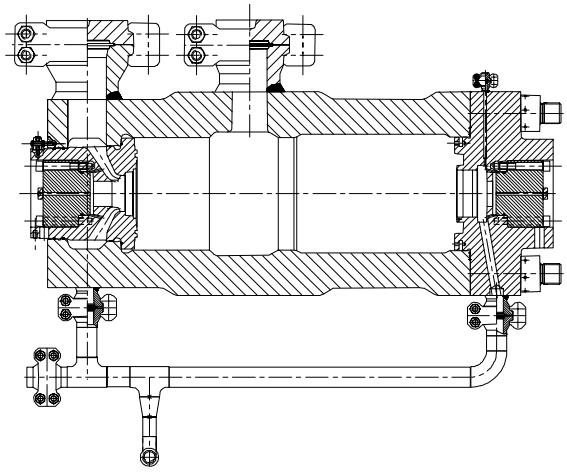

Figure 53. Hydrostatic Pressure Test Assembly.

Hydraulic Performance Test

The prototype pump was set up on the manufacturer's test bed using all their test equipment including the electric motor (Figure 54). A torque-measuring device was attached to the coupling between pump and driver for measuring the absorbed power. During the performance test, conducted according to the API 610 Standard (1995), the shaft and bearing housing vibrations and the bearing temperatures were measured besides flow and head. After a small impeller trim, the hydraulic flow-head characteristic (Figure 55), the NPSH, and the efficiency were in conformance with the predicted pump curve and within the tolerance of the standard (Table 13).

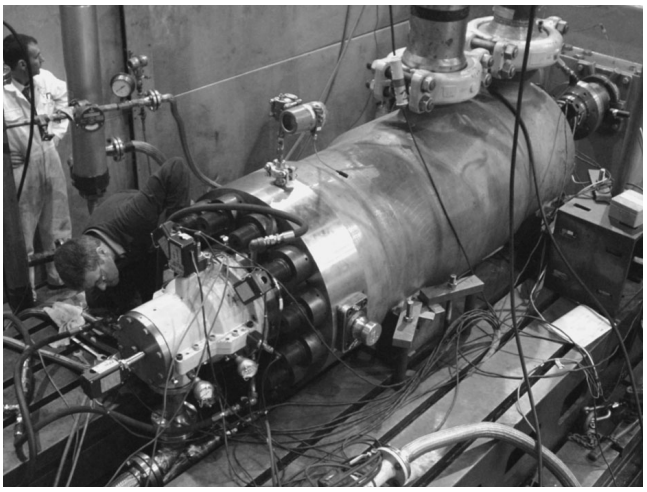

Figure 54. Prototype Under Performance Test.

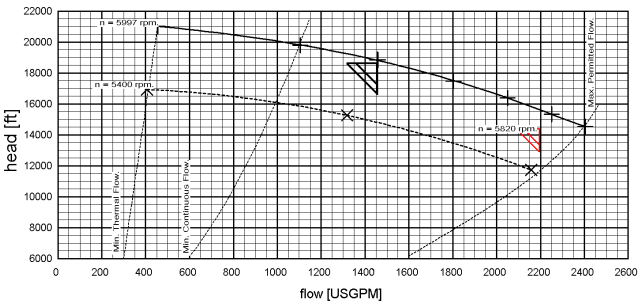

Figure 55. Performance Test Characteristic.

Table 13. Performance Test Data.

Operating point	rated (1)	rated (2)
Speed (rpm)	5820	5997
Flow (m^3/h), (GPM)	497.4 (2190)	331.14 (1458)
Head (m), (ft)	4389 (14,400)	5674 (18,615)
Efficiency (%)	78	75.1
NPSH (m), (ft)	39.6 (130)	21.5 (70.5)

CONCLUSION

The successful completion of all prototype testing proved the integrity of the chosen design. It could be shown that it is possible to push the operating limits of proven designs beyond existing boundaries if sound design practices are followed and if state-of-the-art analytical tools are used with care.

Of course the real proof for a new design will only come during extended operation in the field. Not all adverse field conditions can be simulated during prototype testing on the test bed. Nevertheless, the extensive tests done for this project are far beyond normal factory acceptance testing and will assure safe operation in the field.

The concept chosen by the oil companies to first do a design study, review and evaluate the design thoroughly, and only then build a prototype pump for testing has been proven to be correct. Using this approach, potential risks can be addressed early on, measures to contain these risks can be taken, and design integrity can be assured.

REFERENCES

API Standard 610, 1995, "Centrifugal Pumps for Petroleum, Heavy Duty Chemical and Gas Industry Services," Eighth Edition, American Petroleum Institute, Washington, D.C.

Bolleter, U., et al., 1990, "Causes and Control of Synchronous Vibrations of Multistage Pumps," Seminar on Vibrations in Centrifugal Pumps, Institution of Mechanical Engineers, London, United Kingdom.

DIN 31657, 1996, "Hydrodynamische Radial-Gleitlager im Stationären Betrieb," Deutsches Institut für Normung e. V.

EPRI TR-100980, 1992, Project 1884-10, "Rotordynamic Modeling and Testing of Boiler Feed Pumps," Sulzer Pumps Ltd., Winterthur, Switzerland.

EPRI TR-102102, 1993, "Feedpump Operation and Design Guidelines."

Florjancic, S., 1990, "Annular Seals of High Energy Centrifugal Pumps: A New Theory and Full Scale Measurement of Rotordynamic Coefficients and Hydraulic Friction Factors," ETH Thesis 9087.

Frei, A., Guelich, J., Eichhorn, G., Eberl, J., and McCloskey, T. H., 1990, "Rotordynamic and Dry Running Behavior of a Full Scale Test Boiler Feed Pump," *Proceedings of the Seventh International Pump Users Symposium*, Turbomachinery Laboratory, Texas A&M University, College Station, Texas, pp. 81-92.

ISO 1940-1, 1986, "Mechanical Vibration—Balance Quality Requirements of Rigid Rotors—Part 1: Determination of Permissible Residual Unbalance," International Organization for Standardization, Geneva, Switzerland.

Meuter, P., Bolliger, W., and Schmid, R. K., 2000, "Extension of Pump Life in Abrasive Service," Pump Users International Forum 2000, Pump Congress Karlsruhe.

Weber, J., 1987, "Materials for Seawater Pumps and Related Systems," Sulzer Pumps Publications.

ACKNOWLEDGEMENT

We would like to thank all the many people in the BP Amoco and Sulzer Pumps' organization who contributed to this project to make it a success.